RESEARCH ARTICLE

International Journal of Climatology | RMetS

Analysis of changes in large-scale circulation patterns driving extreme precipitation events over the central-eastern China

Qin Jiang[1,2,3] | Francesco Cioffi[3] | Mario Giannini[3] | Jun Wang[1,2] | Weiyue Li[4]

[1]Key Laboratory of Geographic Information Science (Ministry of Education), East China Normal University, Shanghai, China

[2]School of Geographic Sciences, East China Normal University, Shanghai, China

[3]Dipartimento di Ingegneria Civile, Edile e Ambientale, "La Sapienza" University of Roma, Rome, Italy

[4]School of Environmental and Geographical Sciences, Shanghai Normal University, Shanghai, China

Correspondence
Francesco Cioffi, Dipartimento di Ingegneria Civile, Edile e Ambientale, "La Sapienza" University of Roma, Via Eudossiana 18, 00184 Roma, Italy.
Email: francesco.cioffi@uniroma1.it

Abstract

To an extent, large-scale circulation situations and moisture transport are responsible for extreme precipitation occurrence. The aim of our study is to investigate the possible modifications of circulation patterns (CPs) in driving extreme precipitation over the central-eastern China (CEC). The self-organizing map (SOM) and event synchronization methods are used to link the extreme precipitation events with CPs. Results show that 23% of rain gauges have a significant change point (at the 90% confidence level) in annual extreme precipitation from 1960 to 2015. Based on the identified change points, we classified the data into two periods, that is, 1960–1989 and 1990–2015. Overall, CPs characterized by obvious positive anomalies of 500 hPa geopotential height over the Eastern Eurasia continent and negative values over the surrounding oceans are highly synchronized with extreme precipitation events. During 1990–2015, the predominant CPs are more related to the extreme precipitation with enhanced event synchronization. We found that the CP changes produce an increase in extreme precipitation frequency from 1960–1989 to 1990–2015.

KEYWORDS
circulation patterns, event synchronization, extreme precipitation, integrated vapour transport, self-organizing map

1 | INTRODUCTION

Extensive evidence indicates that extreme precipitation tends to intensify with global warming (Fowler and Kilsby, 2003; Zhan et al., 2020; IPCC, 2021). As a consequence of anthropogenic forcing due to greenhouse gas emissions, an increase of atmospheric water vapour content is expected to contribute to more intense and

frequent precipitation extremes (Allan and Soden, 2008; Min et al., 2011). However, at the scale of specific geographic area, regional precipitation patterns diverge greatly and showing heterogeneity characteristics because of specific atmospheric synoptic situation (Risbey et al., 2013), as well as of the local thermodynamic environment (Ma et al., 2018). For example, changes in regional precipitation patterns over the central Europe from 1950 to 2018 were related to the prevailing atmospheric configurations, that is, the low-pressure or trough systems occurred along this area (Hoffmann and Spekat, 2021).

Generally speaking, large-scale atmospheric circulation patterns (CPs) reflected by geopotential height or sea-level pressure have a broadly dynamic forcing on mesoscale rainfall systems and shapes the processes of extreme events and their subsequent effects (Espinoza et al., 2015; Imada et al., 2020; Moustakis et al., 2020). In previous studies, extreme precipitation in Europe (Haylock and Goodess, 2004), Africa (Rapolaki et al., 2019; Nkunzimana et al., 2020), East Asia (Hu et al., 2019), North America (Schlef et al., 2019) and its connection to the atmospheric circulation have been investigated. Cipolla et al. (2020) analysed rainfall annual maxima events between 1928 and 2016 over Sicily, Italy. The results showed that most events were related to a dominant circulation mode. Ai and Qian (2020) examined the heavy precipitation event of July 2018 in Japan and concluded that the signal of CP anomalies have large potential in understanding heavy precipitation features. Ullah et al. (2021) also pointed out that most of the extreme monsoon precipitation were related to the leading CP in Pakistan. Undoubtedly, robust identification of CPs is essential to understand the links between regional weather and synoptic drivers.

In recent years, objective weather classification technique has been utilized to identify the CPs or circulation anomalies (Bissolli and Dittmann, 2001; Piotrowicz and Ciaranek, 2020). Specifically, CPs extracted from reanalysis or observation data over different spatial domain sizes are corresponding to particular weather conditions, for example, extreme rainfall (Marquardt Collow et al., 2016), drought (Odoulami et al., 2021), or high temperature (Yu et al., 2020) in order to reveal the interactions between circulation anomalies and climatological parameters. Self-organizing map (SOM) is an unsupervised neural network method of objective classification (Kohonen, 1998; Kiang, 2001; Ghaseminezhad and Karami, 2011), superior to the based feature extraction methods, like principal component analysis (PCA; Astel et al., 2007) and empirical orthogonal functions (EOF; Liu and Weisberg, 2005) in interpreting the

physical behaviour of a yielded circulation field. Rousi et al. (2015) evaluated the PCA and SOM methods in recognizing the teleconnection patterns of the winter 500 hPa geopotential height anomalies over Europe. Their comparison suggested that SOM could be the better choice in visualizing less pronounced patterns, especially for complex and diverse data. Consequently, SOM has been commonly used in related research (Nguyen-Le et al., 2017; Olmo and Bettolli, 2021). Agel et al. (2018) explored the links between tropopause height and extreme precipitation by using both the SOM and k-means clustering algorithms. Swales et al. (2016) used SOM method to relate localized extreme precipitation events to the synoptic conditions identified by vertically integrated water vapour transport (IVT) over the western United States. They demonstrated that about 70% of extreme precipitation were related to infrequent circulation patterns.

Meteorologically, atmospheric moisture transport is also a predominant factor indispensable for extreme precipitation events to sustain their development and evolution (Stohl and James, 2004; Feng and Zhou, 2012; Liu et al., 2020). At current, several approaches have been designed to identify the atmospheric water vapour and its trajectory path information. For example, the data-driven atmospheric dispersion modelling systems (e.g., HYSPLIT, Stein et al., 2015; FLEXPART, Pisso et al., 2019) by recognizing moist air parcel trajectories based on Lagrangian models. Additionally, another alternative way is to adopt the quantitative indicators, like vertically integrated water vapour transport (IVT; Kim and Alexander, 2015; Ralph et al., 2019) or vertically integrated water vapour content (IWV; Cordeira et al., 2017; McClenny et al., 2020) to retrieve the atmospheric rivers (ARs). Previous studies highlighted ARs are long, narrow, and fast-flowing water vapour belts (Zhu and Newell, 1994; Zhu and Newell, 1998), which responsible for the majority of the poleward moisture transport (Dacre et al., 2015; Lavers and Villarini, 2015; Barth et al., 2017; Payne et al., 2020). Moreover, the totals, intensities, and durations of regional extreme precipitation are strongly related to the ARs activities (Waliser and Guan, 2017), especially over the East Asia (Cheng et al., 2021), the west coast of Europe (Whan et al., 2020), and United States (Lamjiri et al., 2017; Gershunov et al., 2019). Prince et al. (2021) found that extreme IVT values were associated with hazardous AR events and more conducive to extreme precipitation. Eiras-Barca et al. (2021) also confirmed that intense IVT composites were expected with higher amounts of precipitation. Overall, the quantitative estimates based on IVT provide an effective indicator to characterize the AR events. In this manuscript, IVT composites were

considered to quantify the water vapour transport; the links between CPs (identified by SOM) and heavy precipitation (daily precipitation amount exceeding the 95th percentile) were explored by event synchronization following the approach suggested by Conticello et al. (2018, 2020). They found that this approach was effective in identifying the causality between CPs and extreme events occurrence.

The above-described approaches were applied to the central-eastern China (CEC), which is one of the most densely populated regions and often suffering from seriously flooding induced by excessive precipitation (Duan et al., 2016). Due to its geographic location, on the east side of Eurasia facing the Pacific Ocean, allows for large-scale circulation activities, for example, the meridional movement of the Western Pacific Subtropical High (WPSH; Wang et al., 2019) to promoting amounts of water vapour transport from the oceans to further facilitate the formation of precipitation (Huang et al., 2018). Previous studies have proved that most of persistent extreme precipitation events over the CEC were related to two typical circulation configurations, that is, the double- and single-blocking high types (Chen and Zhai, 2014). Moreover, if abnormal circulation combined with stable water vapour transport could cause devastating precipitation events (Xu et al., 2003). For example, the record-breaking extreme rainstorm hit the CEC in 2020 with a maximum accumulated rainfall of 600 mm (Wang et al., 2021). In that case, the extreme event was mainly conditioned by the strengthen westerly jet and strong water vapour transport from the adjacent seas (Li et al., 2021). More importantly, earlier studies revealed that change points can be detected in extreme precipitation over the CEC (Deng et al., 2018) and globe (He and Sheffield, 2020). The identification of synoptic configurations driving possible increased extreme precipitation is fundamental to forecast such events in order to reduce the hydraulic risk.

Overall, the above analysis awakens us to some new questions: (a) Was there a step-change in extreme precipitation frequency in the last decades over the CEC?; (b) Was it related to the CP changes?; and (c) What are the possible causes? To answer those, in this study, we examined the change points in extreme precipitation over the CEC from 1960 to 2015, and used the SOM and event synchronization methods to investigate the links between large-scale atmospheric CPs with changing extreme precipitation. This paper is organized as follows: the used datasets are presented after this section. Section 3 is about the approaches. Detailed results are described in section 4. Finally, discussion and conclusions are presented in sections 5 and 6, respectively.
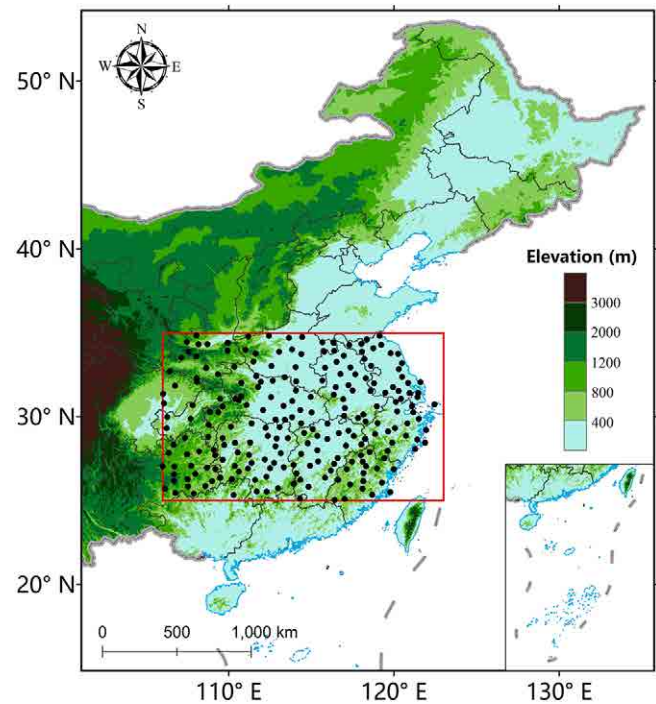

FIGURE 1 Location of study region. Rain gauges are marked with black circles [Colour figure can be viewed at wileyonlinelibrary.com]

2 | DATASETS

Several datasets were used in this study: (a) the daily rain records over the central-eastern China (CEC; $25°–35°$N, $106°–123°$E) were downloaded from the China Meteorological Data Service Centre (http://data.cma.cn/). Available period is January 1960 until December 2015. Figure 1 shows the detailed distribution; (b) the fifth generation atmospheric reanalysis product ERA5, which developed by the European Centre for Medium-Range Weather Forecasts. The used reanalysis variables included geopotential height (z, m) at 500 hPa, eastward (u, m·s^{-1})/northward (v, m·s^{-1}) components of the wind, specific humidity (q, kg·kg^{-1}) from 1,000 to 300 hPa with a spatial resolution of $0.25° \times 0.25°$. Here, for identifying the moisture transport magnitude, we calculated the IVT values (kg·m^{-1}·s^{-1}) for each $0.25°$ grid in the range of $10°$S–$70°$N and $40°$E–$170°$W, referenced to Lavers et al.'s (2012) method,

$$\text{IVT} = \sqrt{\left(\frac{1}{g}\int_{1,000}^{300} qu\,dp\right)^2 + \left(\frac{1}{g}\int_{1,000}^{300} qv\,dp\right)^2}, \quad (1)$$

where g and dp are the acceleration of gravity (9.8 m·s^{-2}) and the difference between two adjacent pressure levels.

3 | METHODS

Our work was inspired by the recent research proposed by Conticello *et al.* (2020) and followed the methods they used for CPs identification. The involved methodology was consisted of five main parts: (a) used the Pettitt test to examine the potential change points in the time series of extreme precipitation from 1960 to 2015 and classified the data into two subperiods; (b) for each gauge, after obtained the binary sequence of extreme precipitation events (1 represents extremes occurred and 0 otherwise), event synchronization was chosen to describe the simultaneities of extreme precipitation occurrence; (c) as the input for the modularity algorithm to divide these rain gauges into some spatially and temporally coherent clusters; (d) SOM was used to identify a finite number of CPs defined on the standardized geopotential height at 500 hPa pressure level in different periods. The daily geopotential height field belongs to which CP was determined by the *k*-nearest neighbour method. Then, event synchronization applied again to identify the synchronized CPs related to the extreme precipitation events for each cluster; (e) used the quantitative partitioning technique to investigate the percentage of extreme precipitation frequency changes attributed to CPs variations.

3.1 | Pettitt test

In this paper, extreme precipitation was defined as the daily precipitation occurred in the top 5% heaviest precipitation events of wet days ($\geq$0.1 mm·day^{-1}) during 1960–2015. For each gauge, the total number of extreme precipitation events and their accumulated rainfall amounts within the 5% range per year can be obtained. Supposed that the step changes occurred in annual extreme precipitation frequency and amount over the interested area, the nonparametric approach Pettitt test aims to discover the shifts in the central tendency across the time series (Pettitt, 1979). Moreover, Pettitt test has the advantage of examining the sensitivity when considering varied record length (Ryberg *et al.*, 2020).

Let $X_1,...,X_t$ and $X_{t+1},...,X_T$ are two samples in a same population, T is the total sample size. The nonparametric statistic K_T can be defined as

$$K_T = \max |U_{t,T}|, 1 \leq t < T, \qquad (2)$$

with

$$U_{t,T} = \sum_{i=1}^{t} \sum_{j=i+1}^{T} \text{sgn}(X_i - X_j), \qquad (3)$$

$$\text{sgn}(X_i - X_j) = \begin{cases} 1 & \text{if } X_i > X_j \\ 0 & \text{if } X_i = X_j \\ -1 & \text{if } X_i < X_j \end{cases}, \qquad (4)$$

where $U_{t,T}$ indicates the Pettitt test index, which is a version of Mann–Whitney two-sample test. The change point of the time series was occurred at the location of K_T that stands the highest value. Given a significance level of α, if the *p*-value is less than the *α* means changes are statistically significant.

Additionally, in order to make the resulting change points more robust, the series of annual extreme precipitation frequency and amount per gauge were undergone the 3-year low-pass filter first to remove the noises. Figure S1, Supporting Information shows the gauges with a statistically significant (at 90% significance level) changing point for annual extreme precipitation frequency and amount. These rain gauges account for 23.26 and 20.61% of total samples. Moreover, the average of the Pettitt test index corresponding to the significant change points are 29.06 and 29.21 (counting since 1960). Therefore, we classified the data into two periods, 1960–1989 and 1990–2015 (before and after the location of the mean change point) to visualize the CPs, respectively.

3.2 | Self-organizing map

We used the SOM toolbox encapsulated in MeteoLab of MATLAB 2021a to cluster the daily geopotential height at 500 hPa into a certain number of CPs over the spatial domain of 10°S–70°N and 40°E–170°W. The identified CPs are called nodes in SOM, which best capture the feature information in observed datasets.

Detailed interpretations of SOM has been presented in previous research (Kohonen, 1998; Kiang, 2001). In short, we only described the basic steps here: (a) Input data preprocessed: before SOM model training, the daily geopotential height at 500 hPa were converted to dimensionless value through the *z*-score standardization method to eliminate the influence of outliers. (b) Training processes: randomly assigned the number and initial weights for nodes. The Euclidean distances between each training sample and the weight vector of nodes were computed to find the best-matching unit, whose weight vector is the closest to the input. The weights of best-matching unit and its neighbouring neurons within the neighbourhood kernel were adjusted iteratively according to the learning rate, in order to let the best-matching unit move closer to the input vector. (c) The output of SOM were evaluated upon two

indicators, quantization error (QE) and topographic error (TE) to determine the optimal size of nodes. QE indicates the average distance between each data point and the node, and TE is the ratio of the data points that the best-matching unit un-adjacent with the secondary. Optimal nodes size depends on the trade-off between low QE and low TE. (d) At last, the classification of daily standardized geopotential height fields during two periods was determined by the *k*-nearest neighbour method (Rajagopalan and Lall, 1999) and produced the binary time sequences per SOM node. For an identified node, 1 represents its occurrence; otherwise 0.

We tested the QE and TE of different node sizes (from 2×2 to 9×9, see Figure S2). The 5×5 node sizes are more reasonable with relatively lower errors.

3.3 | Event synchronization

The event synchronization method proposed by Quiroga *et al.* (2002) and modified by Conticello *et al.* (2018) to measure the synchronization degree and time delay between two binary series. In this study, we used it to quantify the simultaneities of extreme precipitation events among the rain gauges.

Assuming that x_n and y_n, $n = 1, ..., N$ are two binary sequences of extreme precipitation occurrence, t_i^x and t_i^y $(i = 1, ..., m_x; j = 1, ..., m_y)$ represent the time index of recorded extreme events; m_x and m_y denote the total number of recorded extreme events for the two sequences. Preset the time window τ between two sequences, we had the number of event happens in x shortly after it happens in y, that is, $F^\tau(x|y)$.

$$F^\tau(x|y) = \sum_{i=1}^{m_x} W_i, \qquad (5)$$

with

$$W_{ij}^\tau = \begin{cases} 1 & \text{if } \exists \min \left(\left| t_i^x - t_i^y \right| \leq \tau \right) \\ 0 & \text{else} \end{cases}. \qquad (6)$$

Similarly, $F^\tau(y|x)$ can be proved. Then, the synchronization of the extreme events is calculated as follows:

$$S_{x,y}^\tau = \frac{F^\tau(x|y) + F^\tau(y|x)}{m_x + m_y}. \qquad (7)$$

Summarizing, $0 \leq S_{x,y}^\tau \leq 1$. If $S_{x,y}^\tau = 1$, the extreme precipitation events are fully synchronized. Furthermore, the event synchronization method was also used to examine the simultaneous degree between extreme precipitation recorded by rain gauges and the binary sequences per CP. In our study, the time window τ was set to 3 days to quantify the robustness links between two binary sequences.

3.4 | Rain gauges clustering by modularity

In characterizing the structural consistency of extreme precipitation events recorded by rain gauges, a community detection approach was applied. The modularity (Newman, 2004; Newman, 2006) is defined as follows:

$$Q = \frac{1}{2q} \sum_{i,j} \left[A_{ij} - \frac{k_i k_j}{2q} \right] \delta(c_i, c_j), \qquad (8)$$

where Q indicates the modularity, $-0.5 \leq Q < 1$. k_i and k_j are the number of edges for nodes i and j, and $2q$ is the total edges of all nodes. A_{ij} represents the adjacency matrix, ranging between 1 or 0. When nodes i and j belongs to a same group, $\delta(c_i, c_j)$ having a value of 1, otherwise 0.

3.5 | Quantitative partitioning technique

Some previous studies suggested that the changes in extreme precipitation frequency between two different periods could be separated into three components by quantitative partitioning technique (Cassano *et al.*, 2007). Assuming that EP_{all1} is the total frequency of extreme precipitation event in the first period,

$$EP_{all1} = Y_1 * \sum_{i=1}^{C} P_i mf_i, \qquad (9)$$

where Y_1 is the total number of years for initial period, P_i is the annual mean number of CP i occurrences, and mf_i is the annual mean number of extreme precipitation events recorded by this CP. C is the total number of node size. Then, the total extreme events in the second period (EP_{all2}) can be calculated as follows:

$$EP_{all2} = Y_2 * \sum_{i=1}^{C} (P_i mf_i + \Delta P_i mf_i + P_i \Delta mf_i + \Delta P_i \Delta mf_i), \qquad (10)$$

where Y_2 is the total number of years for second period, $\Delta P_i mf_i$ is the component that extreme precipitation

frequency changes attributed to CP i number variation from the initial to the second period. $P_i\Delta mf_i$ and $\Delta P_i\Delta mf_i$ represent the changes attributed to the variations in the average number of extreme precipitation events for a CP and the combined, respectively. Then, for the observed change in mean extreme precipitation frequency for CP i ($\Delta P_i mf_i + P_i\Delta mf_i + \Delta P_i\Delta mf_i$), we can calculate the percentage that the thee three components account for.

4 | RESULTS

4.1 | Identified circulation patterns by SOM

Figure 2 shows the identified CPs by SOM in the two periods, which are arrayed in five columns (labelled A–E and A′–E′, respectively) and five rows (labelled 1–5). The shadow indicates the anomalous fields of standardized geopotential height at 500 hPa, and projected circulation configurations for each CP are plotted in black contours. It is found that these CPs are governed by four distinct nodes (e.g., A1, A5, E1, and E5 in the period of 1960–1989) and some transition types, and their morphological information demonstrates similarity occurs in the adjacent nodes. For the period of 1960–1989, CPs on the diagonals of the top-left and bottom-right have an obvious north–south opposing situation, bounded by 20°N. CPs A4–A5 and B4–B5 are dominated by the positive anomalies over the Eastern Eurasia continent and negative anomalies over the surrounding oceans (e.g., the South China Sea, Bay of Bengal, and the Arabian Sea); CPs D1–D2 and E1–E2 are the opposite. CPs A1 and B1 are controlled by a stable positive anomaly, while negative anomalies can be seen for D5 and E5. Also, the identified CPs in the period of 1990–2015 show similar consistent node characteristics.

In terms of the circulation situation, we can find the WPSH's location (the contour of 5,880 gpm at 500 hPa was used to indicate its extent) and its seasonal movement. For CPs C3–E5 (C′3–E′5), the WPSH are very weak and an obviously cold low-pressure system distributes over the Eastern Siberia. For CPs E2–C1 (E′2–C′1), the increase in 500 hPa geopotential height over the South Pacific, the South China Sea, and India Ocean has enhanced the north–south barometric gradient and promoted the enhancement and northward of WPSH. In addition, the strong WPSH and the blocking high over the Lake Baikal region are mainly circulation systems for A1 and B1 (A′1 and B′1). For CPs A2–B5, the WPSH moves southward and its intensity becomes weak.

Matrix Euclidean distance and correlation coefficient were adopted to investigate the similarities of identified CPs between the two periods, as shown in Figure 3. When compared to the period of 1960–1989, the CPs in 1990–2015 standing at the diagonal have the minimum Euclidean distance and high correlation. This reflects that the category of identified CPs in the latter period generally remains almost unchanged.

Figure 4 shows the composites of daily precipitation anomalies related to per CP. For each rain gauge, this anomaly was achieved by the deviation from their average daily precipitation from 1960 to 2015. Positive value indicates more precipitation than the average, while negative is the opposite. Meanwhile, the time distribution of identified CPs during the two periods is displayed in Figure 5. It can be found that the changes in precipitation anomalies are associated with the evolution of circulation situations, which driven by the north–south propagation of the WPSH. From January to March, the frequent CPs belong to E5–E1 (E′5–E′1) for the period of 1960–1989 (1990–2015) (Figure 5), the WPSH intensity of these CPs are generally weak (Figure 2) and precipitation composites over the CEC are dominated by negative anomalies compared to the climatology (Figure 4). From April to May, the occurrence proportion of CPs C1 and B1 (C′1 and B′1) are the highest, we can find that the intensity of WPSH has strengthened and its ridge line locates at 18°N. At the same time, precipitation over the south CEC also tends to increase. For A1–A5 (A′1–A′5), due to the northward expansion of the WPSH, the rain belt moves from the south to the north CEC from June to August. After that, the WPSH begins to move southward with weakened intensity, and the anomalously high precipitation belt over the CEC also disappeared during October and December.

4.2 | Synchronized circulation patterns with extreme precipitation

In different periods, rain gauges with synchronized characteristics of extreme precipitation were clustered together by the modularity method. The modularity values reached the maximum (i.e., 0.287 of 1960–1989 and 0.279 of 1990–2015, respectively) when the number of clusters set to 4. Figure 6 shows the identified rain gauge clusters over the CEC, which labelled as "East," "West," "North," and "South" according to their geographic location. There is some difference in the clusters in the two periods. Synchronized extreme rainfall in Figure 6a,b seems to show a slight different spatial coherence. Fundamentally, cluster East in the second period extends toward west, while cluster South reduce its extension on the north side.

For each cluster, we calculated the synchronization degree between the binary sequence of extreme
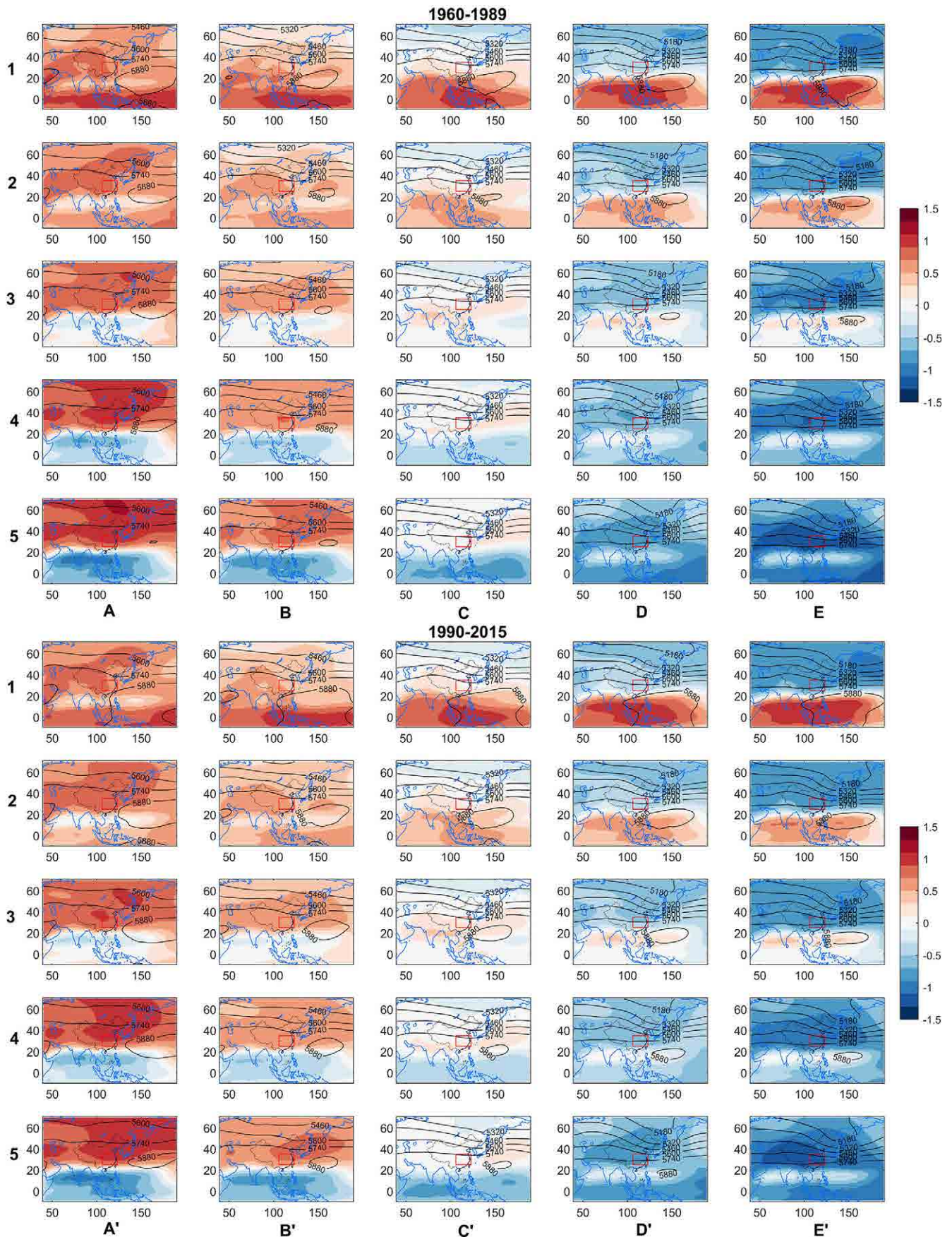
FIGURE 2   The identified CPs of standardized geopotential height at 500 hPa during 1960–1989 and 1990–2015 periods. Shadow indicates anomalous fields of standardized geopotential height at 500 hPa, black contour is the geopotential height composite (unit: gpm) [Colour figure can be viewed at wileyonlinelibrary.com]
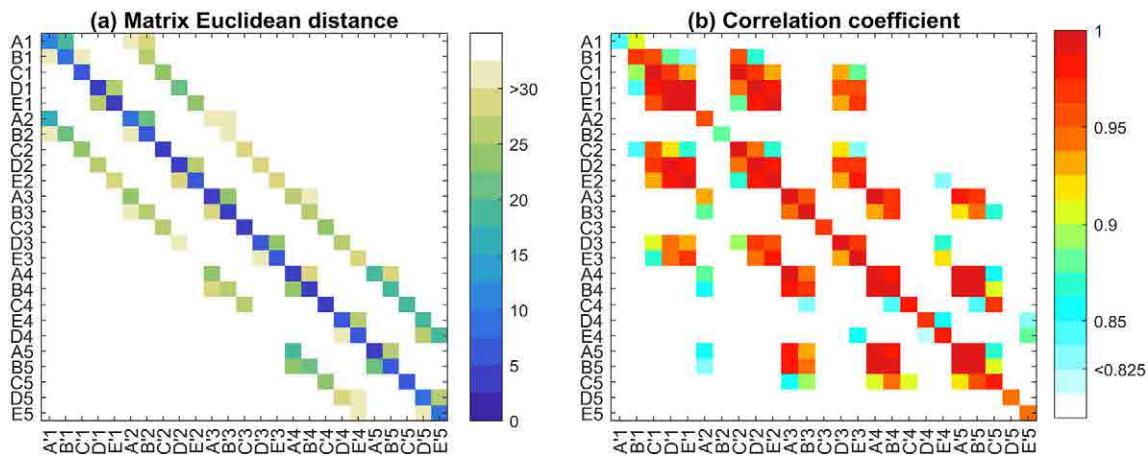
FIGURE 3 Matrix Euclidean distance and correlation coefficient of the CPs between two periods [Colour figure can be viewed at wileyonlinelibrary.com]

precipitation events recorded by each gauge with CPs, respectively. As displayed in Figure 7, the gauge-averaged synchronization matrix allows us to find the CPs highly synchronized with extreme precipitation events across the four clusters. Overall, CPs A1–A5 are strongly synchronized with extreme precipitation over the CEC during 1960–1989. Specifically, CP A4 (A1) has the highest scores with extreme precipitation events for the East (West) cluster, while is A5 (A2) for the North (South) cluster (Figure 7a). In the period of 1990–2015, CPs A′1–A′5, and B′1 are more related to the extreme precipitation in terms of the event synchronization degree (Figure 7b).

To further demonstrate the influence of CP variations and their configuration on extreme precipitation, in the following, we mainly focus on the representative CPs (mean synchronization degree >0.20) analysis. Figure 8 shows the IVT composites and wind fields at 850 hPa for the representative patterns in the two periods. An obvious water vapour channel that originates from the northern Indian Ocean can be found for A1–A5 (A′1–A′5), the IVT values higher than 350 kg·m^{-1}·s^{-1} over the Arabian Sea. Forced by the southwesterly flow, the humidity air mass would affect eastern China via the Indian Peninsula and the Bay of Bengal. Another is the southeast airflow that originates from the western Pacific. Because the wind fields over the CEC for A5 and A′5 are stronger than other CPs, causing the water vapour forced by southwesterly flow would continue toward the north CEC, which can explain the extreme precipitation across the North cluster are more related to CP A5 (A′5) (Figure 8). However, less water vapour is found due to the relatively weak wind fields and IVT intensities of B1 and

B′1, extreme events associate to B1 and B′1 may be less produced. Overall, specific circulation configuration and stable water vapour transport are two factors necessary for the occurrence of extreme precipitation over the CEC.

4.3 | Contribution analysis of extreme precipitation changes

Since the CP categories in the two periods remained the same, here we compared the frequency differences for the same CP type from 1960–1989 to 1990–2015 to analyse how their variations act on extreme precipitation frequency. Figure 9a,b shows the mean annual number of identified CPs in the two periods. Among the representative CPs, B′1, A′2, and A′3 become more frequent in 1990–2015, but a decreased number is found for A′1, A′4, and A′5. Figure 9c indicates the period changes (from 1960–1989 to 1990–2015) in the recorded mean annual frequency of extreme precipitation events (sums of $\Delta P_i m f_i$, $P_i \Delta m f_i$, $\Delta P_i \Delta m f_i$; see Equation (9)) for each CP. The mean number of extreme precipitation events in 1990–2015 for CP A′1 and A′4 are decreased compared to that for A1 and A4 in 1960–1989. Figure 9d shows the percentage that extreme precipitation frequency changes attributed to CP variation. We can find that for the increased extreme precipitation events in A′3 and A′5, 118.7 and 48.67% could be attributed to the relatively increased CP number, respectively. However, for CP A′1, the decreased extreme precipitation event only 26.92% can be attributed to the reduced CP number. For CP A′1 and B′1, these effects on extreme precipitation frequency are relatively weak.
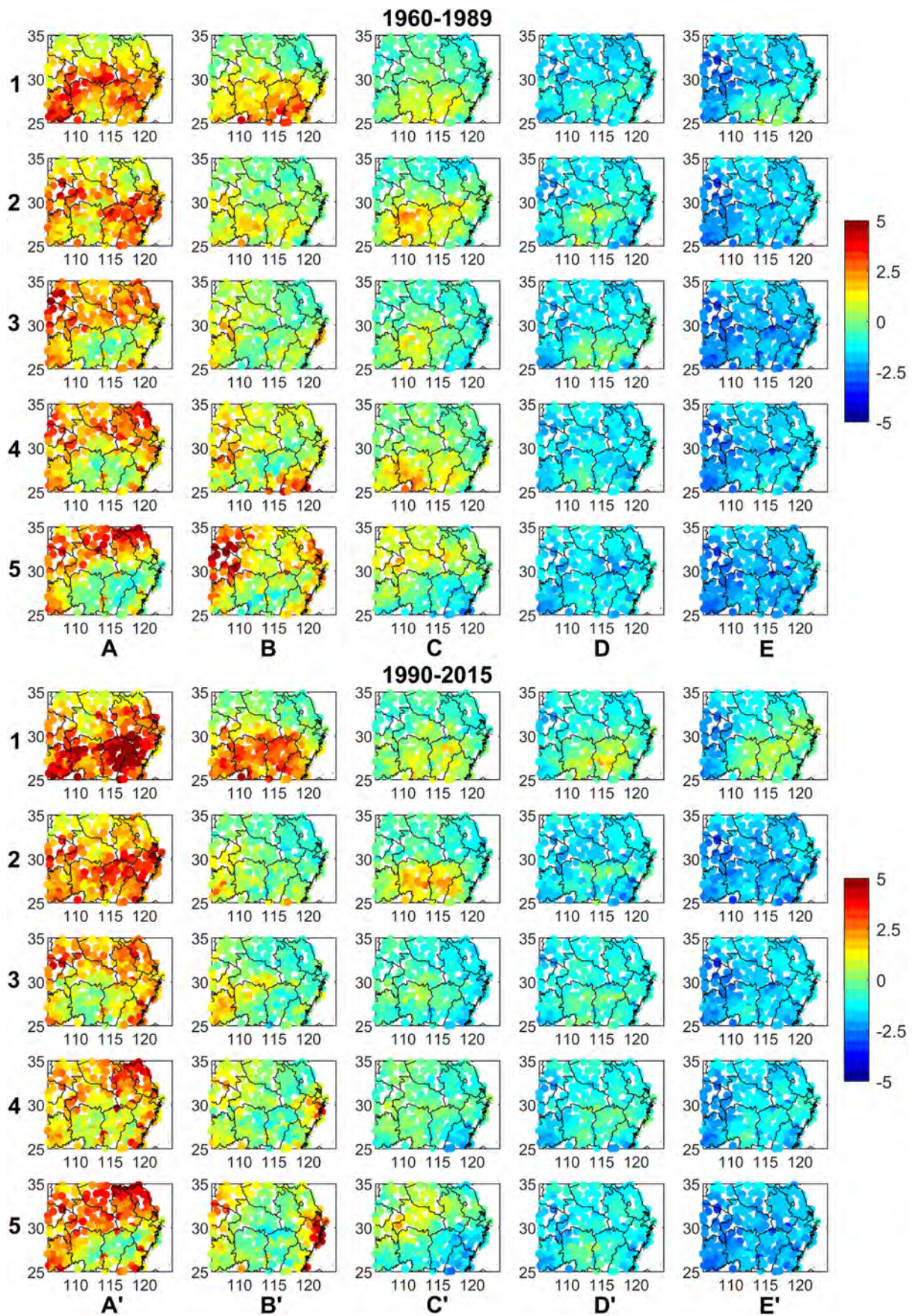
FIGURE 4 Composites of precipitation anomalies for each CP during 1960–1989 and 1990–2015 periods (unit: mm) [Colour figure can be viewed at wileyonlinelibrary.com]
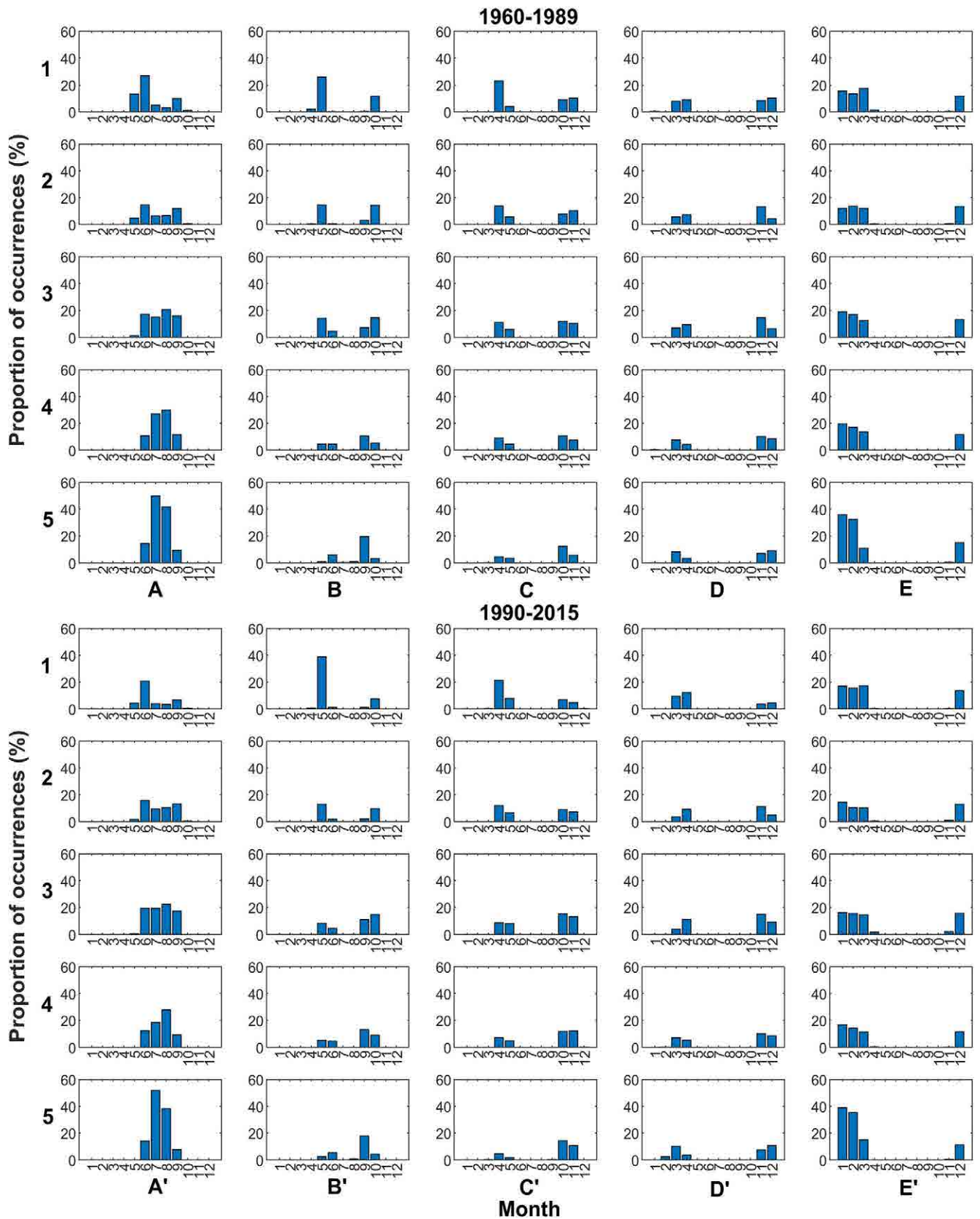
FIGURE 5 Monthly distribution of the identified CPs during 1960–1989 and 1990–2015 periods [Colour figure can be viewed at wileyonlinelibrary.com]
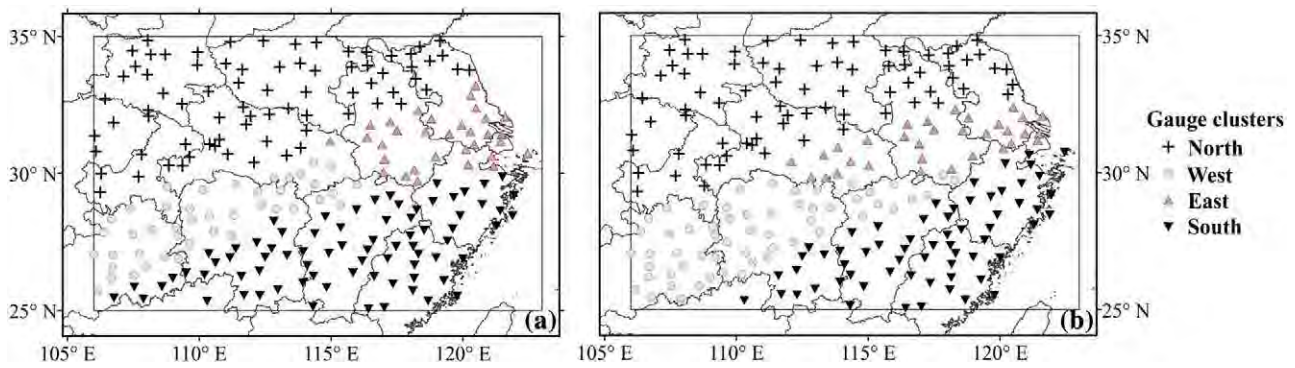
FIGURE 6 Clusters of rain gauges based on modularity method during (a) 1960–1989 and (b) 1990–2015 periods [Colour figure can be viewed at wileyonlinelibrary.com]
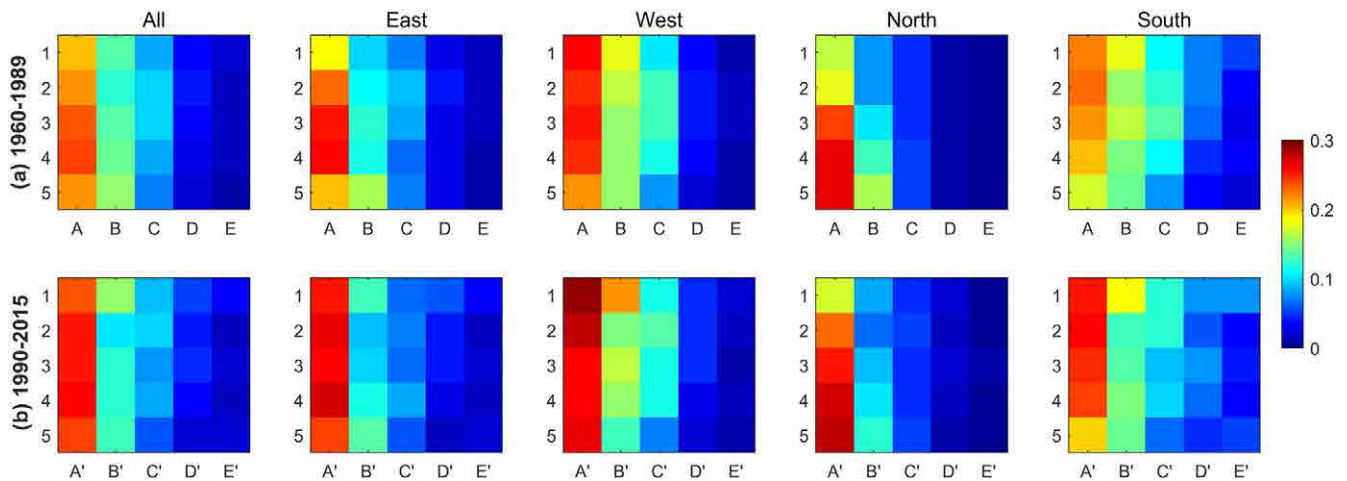

FIGURE 7 Mean synchronization degree for the identified CPs with extreme precipitation events in the whole CEC, East, West, North, and South clusters during (a) 1960–1989 and (b) 1990–2015 periods [Colour figure can be viewed at wileyonlinelibrary.com]

5 | DISCUSSION

Due to more frequent extreme weather events on land, many studies tried to explain this change by analysing their links with large-scale atmospheric circulation variations (Pendergrass, 2018). For example, Swain *et al.* (2016) demonstrated that the variations in zonal gradient of geopotential height at 500 hPa were closely related to seasonal storm tracks in California. Lennard and Hegerl (2015) also found that increase in extreme precipitation was associated with the more frequent key summer circulation modes. In general, the variations in the atmospheric circulation involve intraseasonal, interannual, decadal, and multidecadal timescales. We know that daily changes in the atmospheric horizontal motion are formulated by the gravity and pressure gradient force (e.g., land–sea and pole–equator pressure contrasts) and showed bewildering characteristics; while the year-to-year variabilities are much more manifested (Collins *et al.*, 2010). For example, the intraseasonal periodic

north–south shifts of the WPSH. As it migrates northward and arrives at its most northern climatological-mean position, then southward. Interannual variabilities are often forced by the interactions between the atmosphere and ocean conditions. The most prominent mode is known as the El Niño–Southern Oscillation (ENSO; Wang *et al.*, 1999; Dong *et al.*, 2006). The anomalous sea surface temperature (SST) in the tropical Pacific is responsible for the circulation anomalies in the equatorial Pacific. Previous studies found that the lower-frequency (3–5 year) oscillation in WPSH may be caused by the ENSO cycle (Huang *et al.*, 2020). Moreover, the more slowly varying warm or cool anomalies of SST in the Pacific and Atlantic oceans may also modulate the decadal behaviours of the large-scale circulation activities (Scafetta, 2014; Valdés-Pineda *et al.*, 2018). As the intermediary bridge connecting the ocean, atmospheric circulation could transfer the decadal-scale climate variability of oceanic to affect regional precipitation (Ning *et al.*, 2017; Zhou *et al.*, 2021).
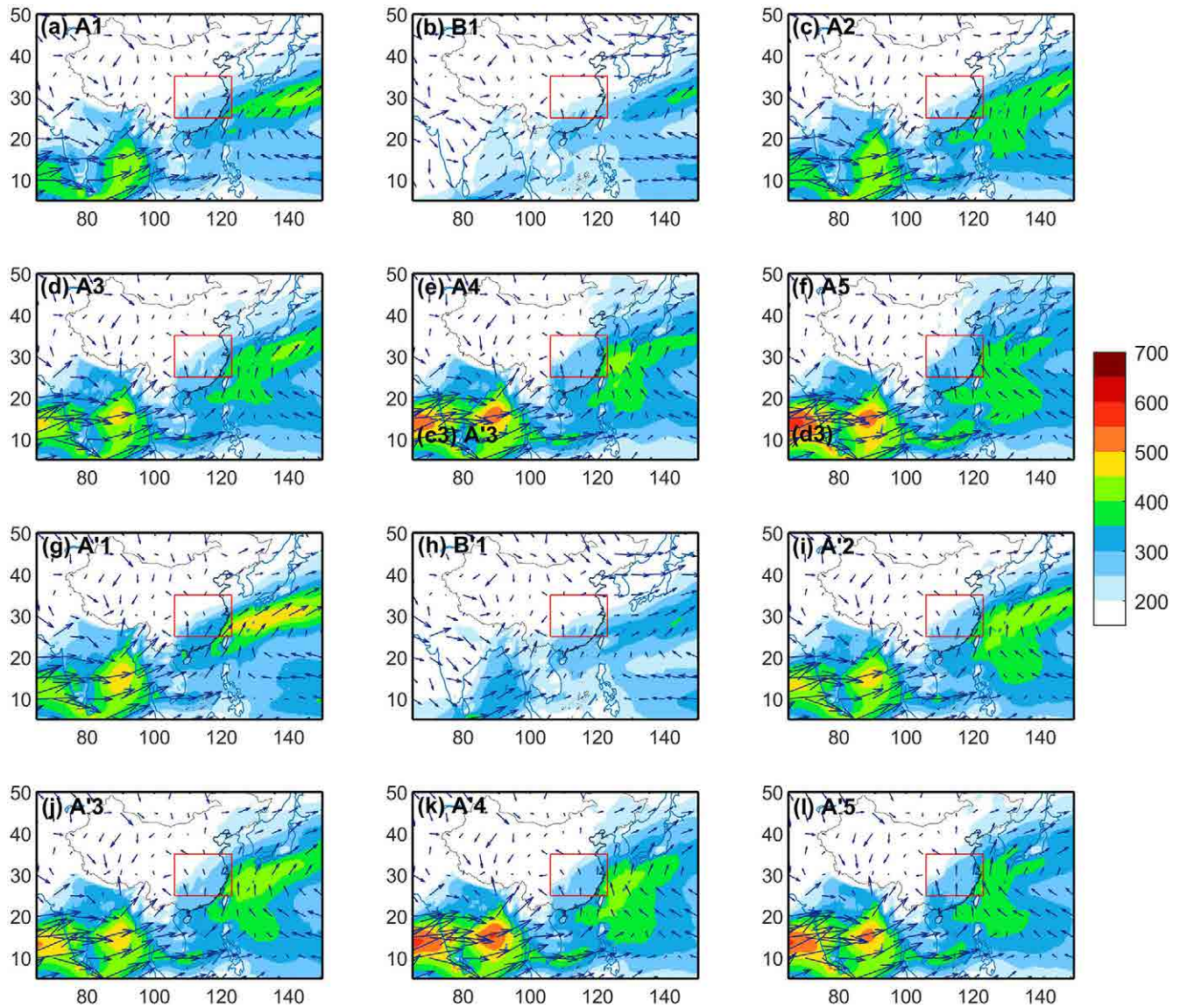
FIGURE 8 IVT composite (kg·m^{-1}·s^{-1}) for the representative CPs during 1960–1989 and 1990–2015 periods, vector arrows are wind composites at 850 hPa [Colour figure can be viewed at wileyonlinelibrary.com]

In this study, the synchronized CPs with extreme precipitation events over the CEC have been identified in the periods of 1960–1989 and 1990–2015. We find that for the increased extreme precipitation events in A′3 and A′5, 118.7 and 48.67% could be attributed to CP changes. However, the possible causes for the representative CPs frequency changes are not well understand. In this section, we selected the Niño3.4 index and two climate indices, that is, the Pacific Decadal Oscillation (PDO) and the Atlantic Multidecadal Oscillation (AMO) to investigate the potential physical mechanism influencing the variations in frequency of the representative CPs. The Niño3.4 index was used to quantify the warm (El Niño) and clod (La Niña) swings of ENSO, and the PDO/AMO indices were defined as the first principal component of monthly

mean SST anomalies in the North Pacific and North Atlantic, respectively.

Figure 10a–c shows the time series of Niño3.4 index, PDO, and AMO indices. The interannual signals of ENSO (or interdecadal variabilities of PDO and AMO) were obtained by the 3-year (12-year) low-pass filter, which allow us to clearly find their phase transition characteristics. The time periodic signals in the annual frequency of representative CPs were decomposed into some subingredients, called intrinsic mode functions (IMFs) by the empirical mode decomposition method (Rilling et al., 2003). Figure 10d–i displays the decomposed IMFs in the annual frequency of representative CPs from 1960 to 2015. Table 1 indicates the correlation coefficients between the decomposed IMFs and the climate
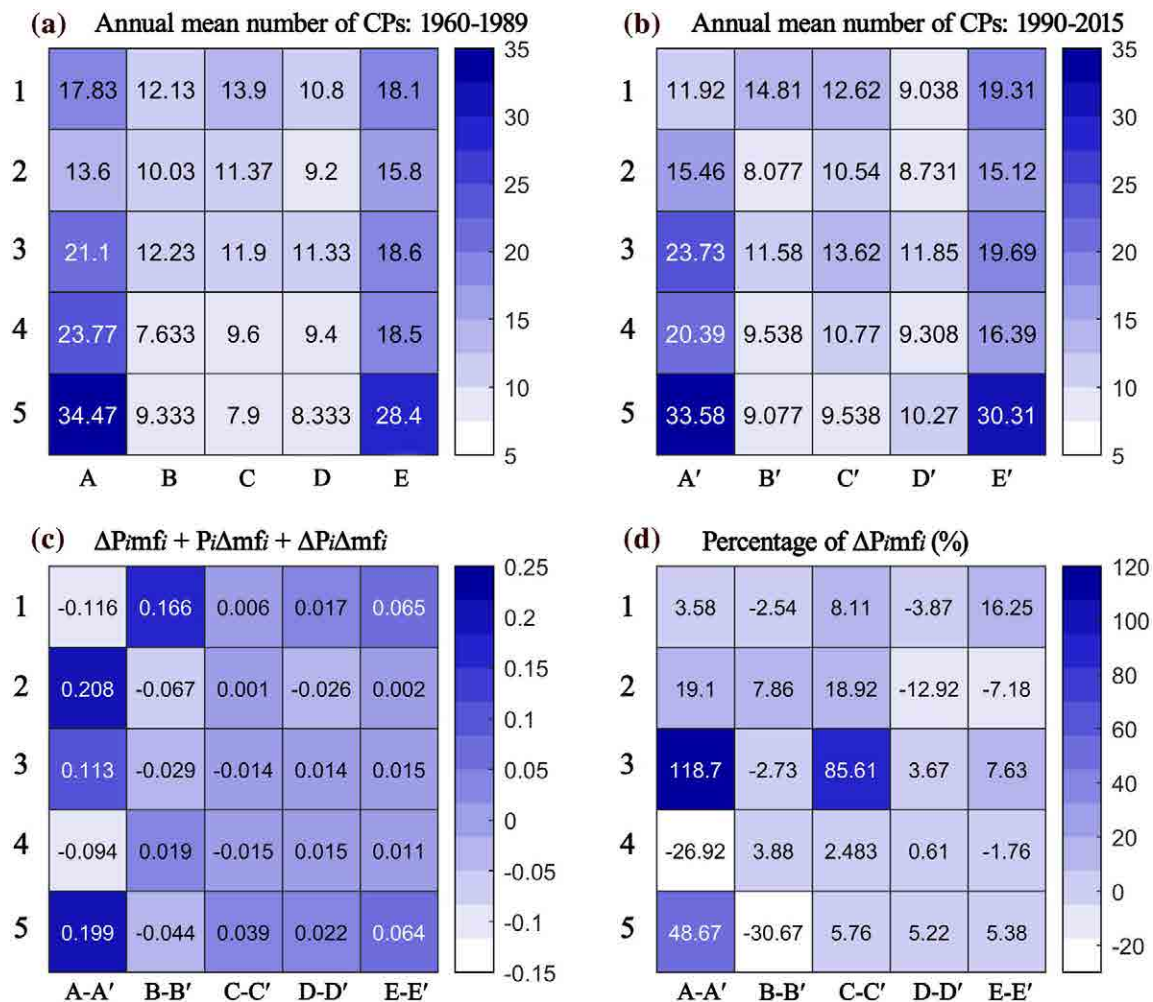
FIGURE 9 Annual mean number of identified CPs in (a) 1960–1989 and (b) 1990–2015. (c) Changes in the recorded annual mean number of extreme precipitation events for each CP and (d) the percentage that extreme precipitation frequency changes attributed to CP frequency variation [Colour figure can be viewed at wileyonlinelibrary.com]

variabilities of ENSO/PDO/AMO. We can find that the 2–4 and 8–10 year quasi-periodic signals (IMF1 and IMF2) in the representative CPs have no correlation with PDO and AMO, but the 2–4 year oscillation in A1–A′1, B1–B′1, and A2–A′2 is positively related to the phase of ENSO (at 99% statistical significance level), for A5–A′5 is the opposite. Previous studies showed that the East Asia summer monsoon (EASM) is tends to stronger when is an El Niño event, and to shift the WPSH more northward; while La Niña is the opposite (Xu *et al.*, 2021). Because CP A5–A′5 is dominated by the relatively weak WPSH (Figure 2), it is natural to have a negative relationship with ENSO.

The 20–25 and 42–50 year periodic oscillations (IMF3 and IMF4) in A1–A′1, B1–B′1, A2–A′2, and A3–A′3 are correlated well with the phase of PDO; while AMO is an important factor affected the

28–30 year (50 year) periodic oscillation in A4–A′4 (A5–A′5). Figure 11 shows the shape, intensity, and location of the summer (i.e., July–August) WPSH in different PDO (AMO) phases. When the PDO is warm (or the AMO is cold), the WPSH tends to be enhanced and more western. The weak WPSH is the opposite. This can explain that the long-period variations of A1–A′1 to A3–A′3 (A5–A′5) are positively (negatively) related to the PDO phase and negatively (positively) to the AMO phase.

Overall, the potential mechanism for CP changes has been discussed in this section. The interannual variations of the representative CPs frequency are associated with ENSO, while the Pacific and Atlantic SSTs modulate the longer periodic. However, as shown by other studies, the amplitude and periodic length of PDO influenced by global warming (Zhang and Delworth, 2016). An increase
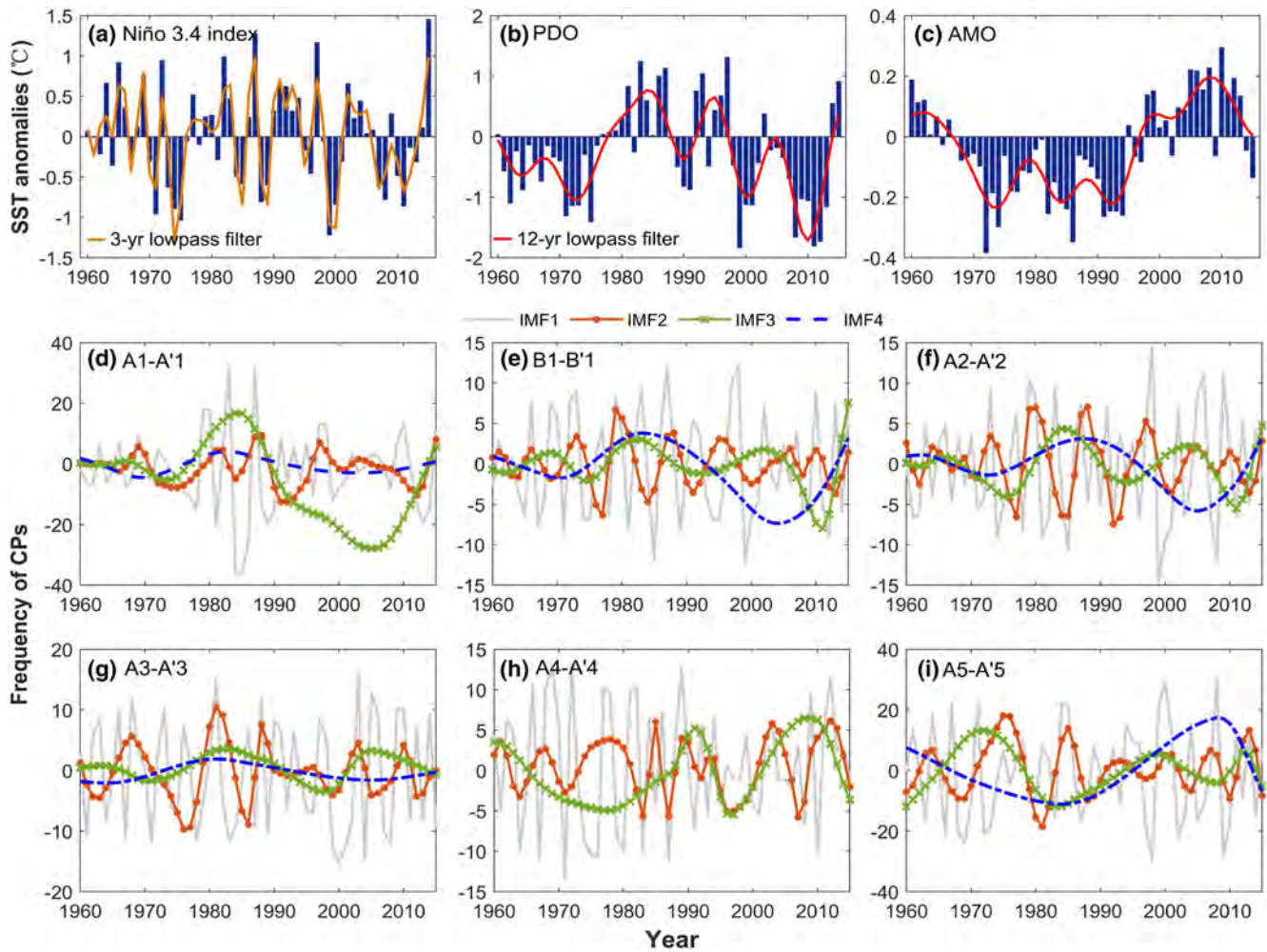
FIGURE 10   Time series of (a) ENSO, (b) PDO, and (c) AMO indices and the decomposed IMFs in the annual frequency of representative CPs from 1960 to 2015 [Colour figure can be viewed at wileyonlinelibrary.com]

TABLE 1   Correlation coefficients between the decomposed IMFs in the annual frequency of representative CPs and the Niño3.4 index, and 12-year low-pass filter of PDO/AMO

	A1–A'1	B1–B'1	A2–A'2	A3–A'3	A4–A'4	A5–A'5
IMF1	**0.44**/−0.08/0.11	**0.57**/0.07/−0.07	**0.42**/0.09/0.02	0.32/−0.02/0.01	0.16/0.02/0.05	**−0.48**/0.11/−0.03
IMF2	0.21/0.27/0.20	0.07/0.12/0.04	0.11/0.00/0.13	0.17/0.11/−0.02	−0.14/−0.16/0.05	−0.29/−0.16/−0.16
IMF3	0.17/**0.49**/**−0.59**	**0.35**/**0.65**/−0.30	0.29/**0.57**/−0.06	0.09/0.20/0.11	−0.02/−0.34/**0.52**	−0.23/**−0.53**/−0.05
IMF4	0.16/**0.62**/−0.37	0.21/**0.57**/−0.67	0.26/**0.58**/−0.64	0.05/**0.54**/−0.73		−0.18/**−0.58**/**0.89**

Note: Bold fonts indicate statistically significant correlation at the 99% confidence levels.

in anthropogenic aerosols also affects atmospheric circulation (Murakami, 2022). The changes in atmospheric circulation and SST results by complex external forcing (e.g., greenhouse gas emission) and inner variability. Identifying the robustness of such links in a warming climate is challenging and it is beyond the scope of this paper.

To sum up, our results confirmed that changes in extreme precipitation frequency can be found from 1960 to 2015 over the CEC, these changes are related to
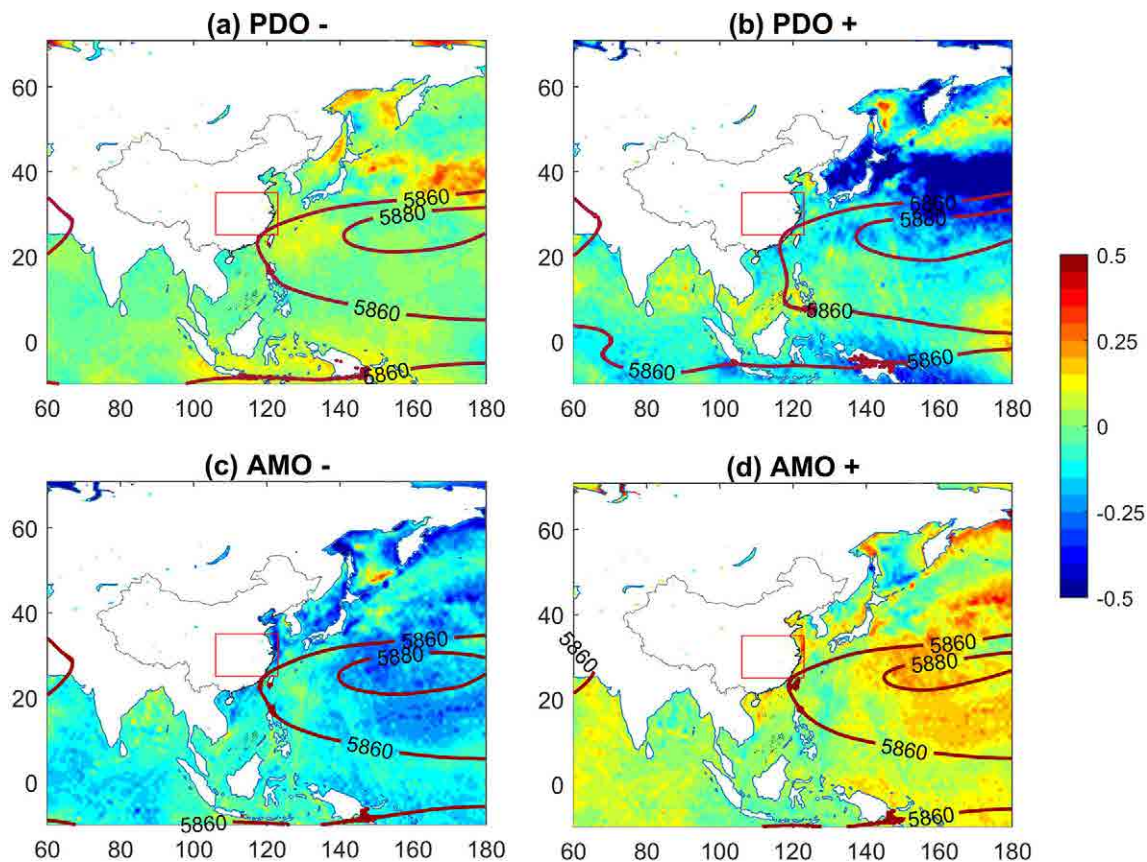
FIGURE 11   Location of 500 hPa WPSH (5,880 contours, unit: gpm) and composite of sea surface temperature anomalies (shadow, unit: °C) in the (a) negative, (b) positive phase of PDO, and the (c) negative, (d) positive phase of AMO during June–August [Colour figure can be viewed at wileyonlinelibrary.com]

circulation patterns activities that can mainly be motivated by the atmospheric and oceanic interactions. This study also provides valuable information for using circulation situations to predict extreme events.

6 | CONCLUSIONS

In this study, we have investigated the characteristics of large-scale circulation patterns and water vapour transport related to the extreme rainfall over the CEC from 1960 to 2015. Based on the changing points of extreme precipitation over the CEC, we objectively choose 5×5 SOM nodes during 1960–1989 and 1990–2015 periods to identify the atmospheric CPs, respectively, based on the standardized geopotential height field at 500 hPa. The SOM and event synchronization methods are effective in classifying and capturing the representative atmospheric circulation, which allows us to find robust links between extreme precipitation events and CPs.

We found that regional extreme precipitation events over the CEC are closely related to the evolution of large-scale CPs. Over the four rain gauge clusters, the predominate CPs that synchronized with extreme precipitation events are different. In addition, water vapour transport also plays an important role in shaping the extreme precipitation over the CEC. Highly intense precipitation over the CEC is primarily associated with the strong southerly moisture flows.

In summary, we have investigated the statistical relationship between circulation patterns and extreme precipitation over the CEC. Existing studies argued that the intensity and frequency of precipitation extremes will increase in a warming climate (Kao and Ganguly, 2011; Papalexiou and Montanari, 2019; Zhan et al., 2020). Based on the findings in this study, one possible direction of future work is to use the methodology presented in this paper to explore the linked relationship and to forecast the occurrence probability of future extreme precipitation under different climate scenarios.

AUTHOR CONTRIBUTIONS
Qin Jiang: Data curation; formal analysis; methodology; writing – original draft. **Francesco Cioffi**: Conceptualization; methodology; supervision; writing – review and editing. **Mario Giannini**: Data curation; methodology.

Jun Wang: Supervision; project administration. **Weiyue Li**: Writing – review and editing.

CONFLICT OF INTEREST

The authors declare no potential conflict of interest.

ORCID

Qin Jiang https://orcid.org/0000-0001-6401-9067

REFERENCES

Agel, L., Barlow, M., Feldstein, S.B. and Gutowski, W.J. (2018) Identification of large-scale meteorological patterns associated with extreme precipitation in the US northeast. *Climate Dynamics*, 50(5), 1819–1839. https://doi.org/10.1007/s00382-017-3724-8.

Ai, Y. and Qian, W. (2020) Anomaly-based synoptic analysis on the heavy rain event of July 2018 in Japan. *Natural Hazards*, 101(3), 651–668. https://doi.org/10.1007/s11069-020-03888-y.

Allan, R.P. and Soden, B.J. (2008) Atmospheric warming and the amplification of precipitation extremes. *Science*, 321(5895), 1481–1484. https://doi.org/10.1126/science.1160787.

Astel, A., Tsakovski, S., Barbieri, P. and Simeonov, V. (2007) Comparison of self-organizing maps classification approach with cluster and principal components analysis for large environmental data sets. *Water Research*, 41(19), 4566–4578. https://doi.org/10.1016/j.watres.2007.06.030.

Barth, N.A., Villarini, G., Nayak, M.A. and White, K. (2017) Mixed populations and annual flood frequency estimates in the western United States: the role of atmospheric rivers. *Water Resources Research*, 53(1), 257–269. https://doi.org/10.1002/2016WR019064.

Bissolli, P. and Dittmann, E. (2001) The objective weather type classification of the German weather service and its possibilities of application to environmental and meteorological investigations. *Meteorologische Zeitschrift*, 10(4), 253–260. https://doi.org/10.1127/0941-2948/2001/0010-0253.

Cassano, J.J., Uotila, P., Lynch, A.H. and Cassano, E.N. (2007) Predicted changes in synoptic forcing of net precipitation in large Arctic river basins during the 21st century. *Journal of Geophysical Research Biogeosciences*, 112, G04S49. https://doi.org/10.1029/2006JG000332.

Chen, Y. and Zhai, P.M. (2014) Two types of typical circulation pattern for persistent extreme precipitation in central-eastern China. *Quarterly Journal of the Royal Meteorological Society*, 140(682), 1467–1478. https://doi.org/10.1002/qj.2231.

Cheng, T.F., Lu, M.Q. and Dai, L. (2021) Moisture channels and pre-existing weather systems for East Asian rain belts. *npj Climate and Atmospheric Science*, 4(1), 32. https://doi.org/10.1038/s41612-021-00187-6.

Cipolla, G., Francipane, A. and Noto, L.V. (2020) Classification of extreme rainfall for a Mediterranean region by means of atmospheric circulation patterns and reanalysis data. *Water Resources Management*, 34(10), 3219–3235. https://doi.org/10.1007/s11269-020-02609-1.

Collins, M., An, S.-I., Cai, W., Ganachaud, A., Guilyardi, E., Jin, F.-F., Jochum, M., Lengaigne, M., Power, S. and Timmermann, A. (2010) The impact of global warming on the tropical Pacific Ocean and El Niño. *Nature Geoscience*, 3(6), 391–397. https://doi.org/10.1038/ngeo868.

Conticello, F.R., Cioffi, F., Lall, U. and Merz, B. (2020) Synchronization and delay between circulation patterns and high streamflow events in Germany. *Water Resources Research*, 56(4), e2019WR025598. https://doi.org/10.1029/2019WR025598.

Conticello, F.R., Cioffi, F., Merz, B. and Lall, U. (2018) An event synchronization method to link heavy rainfall events and large-scale atmospheric circulation features. *International Journal of Climatology*, 38(3), 1421–1437. https://doi.org/10.1002/joc.5255.

Cordeira, J.M., Ralph, F.M., Martin, A., Gaggini, N., Spackman, J. R., Neiman, P.J., Rutz, J.J. and Pierce, R. (2017) Forecasting atmospheric rivers during CalWater 2015. *Bulletin of the American Meteorological Society*, 98(3), 449–459. https://doi.org/10.1175/BAMS-D-15-00245.1.

Dacre, H.F., Clark, P.A., Martinez-Alvarado, O., Stringer, M.A. and Lavers, D.A. (2015) How do atmospheric rivers form? *Bulletin of the American Meteorological Society*, 96(8), 1243–1255. https://doi.org/10.1175/BAMS-D-14-00031.1.

Deng, Y., Jiang, W.G., He, B., Chen, Z. and Jia, K. (2018) Change in intensity and frequency of extreme precipitation and its possible teleconnection with large-scale climate index over the China from 1960 to 2015. *Journal of Geophysical Research: Atmospheres*, 123(4), 2068–2081. https://doi.org/10.1002/2017JD027078.

Dong, B., Sutton, R.T. and Scaife, A.A. (2006) Multidecadal modulation of El Niño–Southern Oscillation (ENSO) variance by Atlantic Ocean sea surface temperatures. *Geophysical Research Letters*, 33, L08705. https://doi.org/10.1029/2006GL025766.

Duan, W.L., He, B., Nover, D., Fan, J.L., Yang, G.S., Chen, W., Meng, H.F. and Liu, C.M. (2016) Floods and associated socioeconomic damages in China over the last century. *Natural Hazards*, 82(1), 401–413. https://doi.org/10.1007/s11069-016-2207-2.

Eiras-Barca, J., Ramos, A.M., Algarra, I., Vázquez, M., Dominguez, F., Miguez-Macho, G., Nieto, R., Gimeno, L., Taboada, J. and Ralph, F.M. (2021) European west coast atmospheric rivers: a scale to characterize strength and impacts. *Weather and Climate Extremes*, 31, 100305. https://doi.org/10.1016/j.wace.2021.100305.

Espinoza, J.C., Chavez, S., Ronchail, J., Junquas, C., Takahashi, K. and Lavado, W. (2015) Rainfall hotspots over the southern tropical Andes: spatial distribution, rainfall intensity, and relations with large-scale atmospheric circulation. *Water Resources Research*, 51(5), 3459–3475. https://doi.org/10.1002/2014WR016273.

Feng, L. and Zhou, T.J. (2012) Water vapor transport for summer precipitation over the Tibetan Plateau: multidata set analysis. *Journal of Geophysical Research: Atmospheres*, 117, D20114. https://doi.org/10.1029/2011JD017012.

Fowler, H.J. and Kilsby, C.G. (2003) Implications of changes in seasonal and annual extreme rainfall. *Geophysical Research Letters*, 30(13), 1720. https://doi.org/10.1029/2003GL017327.

Gershunov, A., Shulgina, T., Clemesha, R.E.S., Guirguis, K., Pierce, D.W., Dettinger, M.D., Lavers, D.A., Cayan, D.R., Polade, S.D., Kalansky, J. and Ralph, F.M. (2019) Precipitation regime change in Western North America: the role of atmospheric rivers. *Scientific Reports*, 9(1), 9944. https://doi.org/10.1038/s41598-019-46169-w.

Ghaseminezhad, M.H. and Karami, A. (2011) A novel self-organizing map (SOM) neural network for discrete groups of data clustering. *Applied Soft Computing*, 11(4), 3771–3778. https://doi.org/10.1016/j.asoc.2011.02.009.

Haylock, M.R. and Goodess, C.M. (2004) Interannual variability of European extreme winter rainfall and links with mean large-scale circulation. *International Journal of Climatology*, 24(6), 759–776. https://doi.org/10.1002/joc.1033.

He, X.G. and Sheffield, J. (2020) Lagged compound occurrence of droughts and pluvials globally over the past seven decades. *Geophysical Research Letters*, 47(14), e2020GL087924. https://doi.org/10.1029/2020GL087924.

Hoffmann, P. and Spekat, A. (2021) Identification of possible dynamical drivers for long-term changes in temperature and rainfall patterns over Europe. *Theoretical and Applied Climatology*, 143(1), 177–191. https://doi.org/10.1007/s00704-020-03373-3.

Hu, Y., Deng, Y., Zhou, Z.M., Cui, C.G. and Dong, X.Q. (2019) A statistical and dynamical characterization of large-scale circulation patterns associated with summer extreme precipitation over the middle reaches of Yangtze river. *Climate Dynamics*, 52(9), 6213–6228. https://doi.org/10.1007/s00382-018-4501-z.

Huang, W.Y., He, X.S., Yang, Z.F., Qiu, T.P., Wright, J.S., Wang, B. and Lin, D.Y. (2018) Moisture sources for wintertime extreme precipitation events over south China during 1979–2013. *Journal of Geophysical Research: Atmospheres*, 123(13), 6690–6712. https://doi.org/10.1029/2018JD028485.

Huang, Z., Zhang, W., Geng, X. and Jin, F.-F. (2020) Recent shift in the state of the western Pacific subtropical high due to ENSO change. *Journal of Climate*, 33(1), 229–241. https://doi.org/10.1175/JCLI-D-18-0873.1.

Imada, Y., Kawase, H., Watanabe, M., Arai, M., Shiogama, H. and Takayabu, I. (2020) Advanced risk-based event attribution for heavy regional rainfall events. *npj Climate and Atmospheric Science*, 3(1), 37. https://doi.org/10.1038/s41612-020-00141-y.

IPCC, 2021: Summary for Policymakers. In: Masson-Delmotte, V., Zhai, P., Pirani, A., Connors, S. L., Péan, C., Berger, S., Caud, N., Chen, Y., Goldfarb, L., Gomis, M. I., Huang, M., Leitzell, K., Lonnoy, E., Matthews, J. B. R., Maycock, T. K., Waterfield, T., Yelekçi, O., Yu, R. and Zhou, B. (Eds.) *Climate Change 2021: The Physical Science Basis. Contribution of Working Group I to the Sixth Assessment Report of the Intergovernmental Panel on Climate Change*. Cambridge: Cambridge University Press. In Press. https://doi.org/10.1017/9781009157896.

Kao, S.C. and Ganguly, A.R. (2011) Intensity, duration, and frequency of precipitation extremes under 21st-century warming scenarios. *Journal of Geophysical Research: Atmospheres*, 116, D16119. https://doi.org/10.1029/2010JD015529.

Kiang, M.Y. (2001) Extending the Kohonen self-organizing map networks for clustering analysis. *Computational Statistics & Data Analysis*, 38(2), 161–180. https://doi.org/10.1016/S0167-9473(01)00040-8.

Kim, H.-M. and Alexander, M.A. (2015) ENSO's modulation of water vapor transport over the Pacific–North American region. *Journal of Climate*, 28(9), 3846–3856. https://doi.org/10.1175/JCLI-D-14-00725.1.

Kohonen, T. (1998) The self-organizing map. *Neurocomputing*, 21(1), 1–6. https://doi.org/10.1016/S0925-2312(98)00030-7.

Lamjiri, M.A., Dettinger, M.D., Ralph, F.M. and Guan, B. (2017) Hourly storm characteristics along the U.S. West Coast: role of atmospheric rivers in extreme precipitation. *Geophysical Research Letters*, 44(13), 7020–7028. https://doi.org/10.1002/2017GL074193.

Lavers, D.A. and Villarini, G. (2015) The contribution of atmospheric rivers to precipitation in Europe and the United States. *Journal of Hydrology*, 522, 382–390. https://doi.org/10.1016/j.jhydrol.2014.12.010.

Lavers, D.A., Villarini, G., Allan, R.P., Wood, E.F. and Wade, A.J. (2012) The detection of atmospheric rivers in atmospheric reanalyses and their links to British winter floods and the large-scale climatic circulation. *Journal of Geophysical Research: Atmospheres*, 117, D20106. https://doi.org/10.1029/2012JD018027.

Lennard, C. and Hegerl, G. (2015) Relating changes in synoptic circulation to the surface rainfall response using self-organising maps. *Climate Dynamics*, 44(3), 861–879. https://doi.org/10.1007/s00382-014-2169-6.

Li, C.F., Lu, R.Y., Dunstone, N., Scaife, A.A., Bett, P.E. and Zheng, F. (2021) The seasonal prediction of the exceptional Yangtze River rainfall in summer 2020. *Advances in Atmospheric Sciences*, 38(12), 2055–2066. https://doi.org/10.1007/s00376-021-1092-0.

Liu, B.J., Tan, X.Z., Gan, T.Y., Chen, X.H., Lin, K.R., Lu, M.Q. and Liu, Z.Y. (2020) Global atmospheric moisture transport associated with precipitation extremes: mechanisms and climate change impacts. *WIREs Water*, 7(2), e1412. https://doi.org/10.1002/wat2.1412.

Liu, Y.G. and Weisberg, R.H. (2005) Patterns of ocean current variability on the West Florida Shelf using the self-organizing map. *Journal of Geophysical Research: Oceans*, 110, C06003. https://doi.org/10.1029/2004JC002786.

Ma, Y.Z., Hong, Y., Chen, Y., Yang, Y., Tang, G.Q., Yao, Y.J., Long, D., Li, C.M., Han, Z.Y. and Liu, R.H. (2018) Performance of optimally merged multisatellite precipitation products using the dynamic Bayesian model averaging scheme over the Tibetan Plateau. *Journal of Geophysical Research: Atmospheres*, 123(2), 814–834. https://doi.org/10.1002/2017JD026648.

Marquardt Collow, A.B., Bosilovich, M.G. and Koster, R.D. (2016) Large-scale influences on summertime extreme precipitation in the northeastern United States. *Journal of Hydrometeorology*, 17(12), 3045–3061. https://doi.org/10.1175/JHM-D-16-0091.1.

McClenny, E.E., Ullrich, P.A. and Grotjahn, R. (2020) Sensitivity of atmospheric river vapor transport and precipitation to uniform sea surface temperature increases. *Journal of Geophysical Research: Atmospheres*, 125(21), e2020JD033421. https://doi.org/10.1029/2020JD033421.

Min, S.-K., Zhang, X.B., Zwiers, F.W. and Hegerl, G.C. (2011) Human contribution to more-intense precipitation extremes. *Nature*, 470(7334), 378–381. https://doi.org/10.1038/nature09763.

Moustakis, Y., Onof, C.J. and Paschalis, A. (2020) Atmospheric convection, dynamics and topography shape the scaling pattern of hourly rainfall extremes with temperature globally. *Communications Earth & Environment*, 1(1), 11. https://doi.org/10.1038/s43247-020-0003-0.

Murakami, H. (2022) Substantial global influence of anthropogenic aerosols on tropical cyclones over the past 40 years. *Science Advances*, 8(19), eabn9493. https://doi.org/10.1126/sciadv.abn9493.

Newman, M.E.J. (2004) Fast algorithm for detecting community structure in networks. *Physical Review E*, 69(6), 066133. https://doi.org/10.1103/PhysRevE.69.066133.

Newman, M.E.J. (2006) Modularity and community structure in networks. *Proceedings of the National Academy of Sciences*, 103(23), 8577–8582. https://doi.org/10.1073/pnas.0601602103.

Nguyen-Le, D., Yamada, T.J. and Tran-Anh, D. (2017) Classification and forecast of heavy rainfall in northern Kyushu during Baiu season using weather pattern recognition. *Atmospheric Science Letters*, 18(8), 324–329. https://doi.org/10.1002/asl.759.

Ning, L., Liu, J. and Wang, B. (2017) How does the South Asian High influence extreme precipitation over eastern China? *Journal of Geophysical Research: Atmospheres*, 122(8), 4281–4298. https://doi.org/10.1002/2016JD026075.

Nkunzimana, A., Bi, S.B., Alriah, M.A.A., Zhi, T. and Kur, N.A.D. (2020) Diagnosis of meteorological factors associated with recent extreme rainfall events over Burundi. *Atmospheric Research*, 244, 105069. https://doi.org/10.1016/j.atmosres.2020.105069.

Odoulami, R.C., Wolski, P. and New, M. (2021) A SOM-based analysis of the drivers of the 2015–2017 Western Cape drought in South Africa. *International Journal of Climatology*, 41(S1), E1518–E1530. https://doi.org/10.1002/joc.6785.

Olmo, M.E. and Bettolli, M.L. (2021) Extreme daily precipitation in southern South America: statistical characterization and circulation types using observational datasets and regional climate models. *Climate Dynamics*, 57(3), 895–916. https://doi.org/10.1007/s00382-021-05748-2.

Papalexiou, S.M. and Montanari, A. (2019) Global and regional increase of precipitation extremes under global warming. *Water Resources Research*, 55(6), 4901–4914. https://doi.org/10.1029/2018WR024067.

Payne, A.E., Demory, M.-E., Leung, L.R., Ramos, A.M., Shields, C.A., Rutz, J.J., Siler, N., Villarini, G., Hall, A. and Ralph, F.M. (2020) Responses and impacts of atmospheric rivers to climate change. *Nature Reviews Earth & Environment*, 1(3), 143–157. https://doi.org/10.1038/s43017-020-0030-5.

Pendergrass, A.G. (2018) What precipitation is extreme? *Science*, 360(6393), 1072–1073. https://doi.org/10.1126/science.aat1871.

Pettitt, A.N. (1979) A non-parametric approach to the change-point problem. *Journal of the Royal Statistical Society: Series C (Applied Statistics)*, 28(2), 126–135. https://doi.org/10.2307/2346729.

Piotrowicz, K. and Ciaranek, D. (2020) A selection of weather type classification systems and examples of their application. *Theoretical and Applied Climatology*, 140(1), 719–730. https://doi.org/10.1007/s00704-020-03118-2.

Pisso, I., Sollum, E., Grythe, H., Kristiansen, N.I., Cassiani, M., Eckhardt, S., Arnold, D., Morton, D., Thompson, R.L. and Groot Zwaaftink, C.D. (2019) The Lagrangian particle dispersion model FLEXPART version 10.4. *Geoscientific Model Development*, 12(12), 4955–4997. https://doi.org/10.5194/gmd-12-4955-2019.

Prince, H.D., Cullen, N.J., Gibson, P.B., Conway, J. and Kingston, D.G. (2021) A climatology of atmospheric rivers in New Zealand. *Journal of Climate*, 34(11), 4383–4402. https://doi.org/10.1175/JCLI-D-20-0664.1.

Quiroga, R.Q., Kreuz, T. and Grassberger, P. (2002) Event synchronization: a simple and fast method to measure synchronicity and time delay patterns. *Physical Review E*, 66(4), 041904. https://doi.org/10.48550/arXiv.nlin/0202065.

Rajagopalan, B. and Lall, U. (1999) A k-nearest-neighbor simulator for daily precipitation and other weather variables. *Water Resources Research*, 35(10), 3089–3101. https://doi.org/10.1029/1999WR900028.

Ralph, F.M., Rutz, J.J., Cordeira, J.M., Dettinger, M., Anderson, M., Reynolds, D., Schick, L.J. and Smallcomb, C. (2019) A scale to characterize the strength and impacts of atmospheric rivers. *Bulletin of the American Meteorological Society*, 100(2), 269–289. https://doi.org/10.1175/BAMS-D-18-0023.1.

Rapolaki, R.S., Blamey, R.C., Hermes, J.C. and Reason, C.J.C. (2019) A classification of synoptic weather patterns linked to extreme rainfall over the Limpopo River basin in southern Africa. *Climate Dynamics*, 53(3), 2265–2279. https://doi.org/10.1007/s00382-019-04829-7.

Rilling, G., Flandrin, P. and Goncalves, P. (2003) On empirical mode decomposition and its algorithms. IEEE-EURASIP Workshop on Nonlinear Signal and Image Processing. Grado: IEEER, 3(3), 8–11.

Risbey, J.S., McIntosh, P.C. and Pook, M.J. (2013) Synoptic components of rainfall variability and trends in southeast Australia. *International Journal of Climatology*, 33(11), 2459–2472. https://doi.org/10.1002/joc.3597.

Rousi, E., Anagnostopoulou, C., Tolika, K. and Maheras, P. (2015) Representing teleconnection patterns over Europe: a comparison of SOM and PCA methods. *Atmospheric Research*, 152, 123–137. https://doi.org/10.1016/j.atmosres.2013.11.010.

Ryberg, K.R., Hodgkins, G.A. and Dudley, R.W. (2020) Change points in annual peak streamflows: method comparisons and historical change points in the United States. *Journal of Hydrology*, 583, 124307. https://doi.org/10.1016/j.jhydrol.2019.124307.

Scafetta, N. (2014) Multi-scale dynamical analysis (MSDA) of sea level records versus PDO, AMO, and NAO indexes. *Climate Dynamics*, 43(1), 175–192. https://doi.org/10.1007/s00382-013-1771-3.

Schlef, K.E., Moradkhani, H. and Lall, U. (2019) Atmospheric circulation patterns associated with extreme United States floods identified via machine learning. *Scientific Reports*, 9(1), 7171. https://doi.org/10.1038/s41598-019-43496-w.

Stein, A.F., Draxler, R.R., Rolph, G.D., Stunder, B.J.B., Cohen, M.D. and Ngan, F. (2015) NOAA's HYSPLIT atmospheric transport

and dispersion modeling system. *Bulletin of the American Meteorological Society*, 96(12), 2059–2077. https://doi.org/10.1175/BAMS-D-14-00110.1.

Stohl, A. and James, P. (2004) A Lagrangian analysis of the atmospheric branch of the global water cycle. Part I: method description, validation, and demonstration for the August 2002 flooding in central Europe. *Journal of Hydrometeorology*, 5(4), 656–678. https://doi.org/10.1175/1525-7541(2004)005<0656:ALAOTA>2.0.CO;2.

Swain, D.L., Horton, D.E., Singh, D. and Diffenbaugh, N.S. (2016) Trends in atmospheric patterns conducive to seasonal precipitation and temperature extremes in California. *Science Advances*, 2(4), e1501344. https://doi.org/10.1126/sciadv.1501344.

Swales, D., Alexander, M. and Hughes, M. (2016) Examining moisture pathways and extreme precipitation in the U.S. Intermountain West using self-organizing maps. *Geophysical Research Letters*, 43(4), 1727–1735. https://doi.org/10.1002/2015GL067478.

Ullah, W., Wang, G.J., Lou, D., Ullah, S., Bhatti, A.S., Ullah, S., Karim, A., Hagan, D.F.T. and Ali, G. (2021) Large-scale atmospheric circulation patterns associated with extreme monsoon precipitation in Pakistan during 1981–2018. *Atmospheric Research*, 253, 105489. https://doi.org/10.1016/j.atmosres.2021.105489.

Valdés-Pineda, R., Cañón, J. and Valdés, J.B. (2018) Multi-decadal 40-to 60-year cycles of precipitation variability in Chile (South America) and their relationship to the AMO and PDO signals. *Journal of Hydrology*, 556, 1153–1170. https://doi.org/10.1016/j.jhydrol.2017.01.031.

Waliser, D. and Guan, B. (2017) Extreme winds and precipitation during landfall of atmospheric rivers. *Nature Geoscience*, 10(3), 179–183. https://doi.org/10.1038/ngeo2894.

Wang, H.-J., Zhang, R.-H., Cole, J. and Chavez, F. (1999) El Niño and the related phenomenon Southern Oscillation (ENSO): the largest signal in interannual climate variation. *Proceedings of the National Academy of Sciences of the United States of America*, 96(20), 11071–11072. https://doi.org/10.1073/pnas.96.20.11071.

Wang, L.C., Sun, X.G., Yang, X.Q., Tao, L.F. and Zhang, Z.Q. (2021) Contribution of water vapor to the record-breaking extreme Meiyu rainfall along the Yangtze River valley in 2020. *Journal of Meteorological Research*, 35(4), 557–570. https://doi.org/10.1007/s13351-021-1030-1.

Wang, T.J., Zhong, Z., Sun, Y. and Wang, J. (2019) Impacts of tropical cyclones on the meridional movement of the western Pacific subtropical high. *Atmospheric Science Letters*, 20(5), e893. https://doi.org/10.1002/asl.893.

Whan, K., Sillmann, J., Schaller, N. and Haarsma, R. (2020) Future changes in atmospheric rivers and extreme precipitation in Norway. *Climate Dynamics*, 54(3), 2071–2084. https://doi.org/10.1007/s00382-019-05099-z.

Xu, M., Xu, H., Ma, J. and Deng, J. (2021) Impact of Atlantic multi-decadal oscillation on interannual relationship between ENSO and East Asian early summer monsoon. *International Journal of Climatology*, 41(4), 2860–2877. https://doi.org/10.1002/joc.6994.

Xu, X.D., Miao, Q.J., Wang, J.Z. and Zhang, X.J. (2003) The water vapor transport model at the regional boundary during the Meiyu period. *Advances in Atmospheric Sciences*, 20(3), 333–342. https://doi.org/10.1007/BF02690791.

Yu, B., Lin, H., Kharin, V.V. and Wang, X.L. (2020) Interannual variability of North American winter temperature extremes and its associated circulation anomalies in observations and CMIP5 simulations. *Journal of Climate*, 33(3), 847–865. https://doi.org/10.1175/JCLI-D-19-0404.1.

Zhan, W., He, X.G., Sheffield, J. and Wood, E.F. (2020) Projected seasonal changes in large-scale global precipitation and temperature extremes based on the CMIP5 ensemble. *Journal of Climate*, 33(13), 5651–5671. https://doi.org/10.1175/JCLI-D-19-0311.1.

Zhang, L.P. and Delworth, T.L. (2016) Simulated response of the Pacific Decadal Oscillation to climate change. *Journal of Climate*, 29(16), 5999–6018. https://doi.org/10.1175/JCLI-D-15-0690.1.

Zhou, Z.Q., Xie, S.P. and Zhang, R.H. (2021) Historic Yangtze flooding of 2020 tied to extreme Indian Ocean conditions. *Proceedings of the National Academy of Sciences of the United States of America*, 118(12), e2022255118. https://doi.org/10.1073/pnas.2022255118.

Zhu, Y. and Newell, R.E. (1994) Atmospheric rivers and bombs. *Geophysical Research Letters*, 21(18), 1999–2002. https://doi.org/10.1029/94GL01710.

Zhu, Y. and Newell, R.E. (1998) A proposed algorithm for moisture fluxes from atmospheric rivers. *Monthly Weather Review*, 126(3), 725–735. https://doi.org/10.1175/1520-0493(1998)126<0725:APAFMF>2.0.CO;2.

SUPPORTING INFORMATION

Additional supporting information can be found online in the Supporting Information section at the end of this article.

> **How to cite this article:** Jiang, Q., Cioffi, F., Giannini, M., Wang, J., & Li, W. (2022). Analysis of changes in large-scale circulation patterns driving extreme precipitation events over the central-eastern China. *International Journal of Climatology*, 1–19. https://doi.org/10.1002/joc.7788